# Microstructure–conductivity relationship of $Na_3Zr_2(SiO_4)_2(PO_4)$ ceramics

Sahir Naqash[1-3*], Doris Sebold[1-2], Frank Tietz[1-3], Olivier Guillon[1-3]

1. Forschungszentrum Jülich GmbH, Institute of Energy and Climate Research – Materials Synthesis and Processing (IEK-1), 52425 Jülich, Germany;
2. Jülich Aachen Research Alliance, JARA-ENERGY;
3. Helmholtz-Institute Münster, Forschungszentrum Jülich GmbH, 52425 Jülich, Germany

**Abstract**

The ionic conductivity of solid electrolytes is dependent on synthesis and processing conditions, i.e. powder properties, shaping parameters, sintering time ($t_s$), and sintering temperature ($T_s$). In this study, $Na_3Zr_2(SiO_4)_2(PO_4)$ was sintered at 1200 °C and 1250 °C for 0–10 h and its microstructure and electrical performance were investigated by means of scanning electron microscopy and impedance spectroscopy. After sintering under all conditions, the NASICON-type structure was formed along with $ZrO_2$ as a secondary phase. The microstructure investigation revealed a bimodal particle size distribution and grain growth at both $T_s$. The density of samples increased from 60 % at 1200 °C for 0 h to 93 % at 1250 °C for 10 h. The ionic conductivity of the samples increased with $t_s$ due to densification and grain growth, ranging from 0.13 mS $cm^{-1}$ to 0.71 mS $cm^{-1}$, respectively. The corresponding equivalent circuit fitting for the impedance spectra revealed that grain boundary resistance is the prime factor contributing to the changing conductivity after sintering. The activation energy of the bulk conductivity ($E_{a,bulk}$) remained almost constant (0.26 eV) whereas the activation energy of the total conductivity ($E_a$) exhibited a decreasing trend from 0.37 eV to 0.30 eV for the samples with $t_s$ = 0 h and 10 h,

* Corresponding author: E-mail: s.naqash@fz-juelich.de

Keywords: ionic conductivity, NASICON, microstructure, processing

respectively – both sintered at 1250 °C. In this study, the control of the grain boundaries improved the electrical conductivity by a factor of six.

## 1. Introduction

Sodium super-ionic conductor (NASICON) materials have gained increasing attention in recent years due to a revival of sodium batteries. Aside from the ß-aluminas, NASICON materials are the only group of oxide materials that exhibit very high ionic conductivity. As polycrystalline ceramics, some compositions demonstrate similar ionic conductivity to $Na^+$-ß''-$Al_2O_3$, reaching several mS/cm at room temperature (1-5), and are worth being reconsidered as electrolyte materials in sodium batteries (6-9). $Na_3Zr_2(SiO_4)_2(PO_4)$, hereafter abbreviated as NZSP, is the most commonly studied NASICON material that also has excellent electrical properties (10). The reported conductivity of NZSP varies from $9.2 \times 10^{-5}$ S $cm^{-1}$ (11) to $1.2 \times 10^{-3}$ S $cm^{-1}$ (12) for conventionally sintered ceramic specimens. Spark-plasma-sintered samples attain conductivity of $1.8 \times 10^{-3}$ S $cm^{-1}$ (13). The wide scatter of conductivity data mainly results from the different densities and microstructures of the samples, which are directly related to the processing conditions. In addition, information regarding sample quality i.e., grain size, microstructure and analytical stoichiometries is rarely given in previous publications.

Ceramic processing is the quality-determining step of any polycrystalline material and the main reason for the different total conductivities of NASICON materials (14). More precisely, the quality of a ceramic is determined by the powder properties as well as the shaping and sintering conditions. The powder characteristics (particle size distribution, particle shape, sintering activity) are strongly dependent on the synthesis method, whereas the shape formation (pressing, casting, printing, etc.) and subsequent sintering determine the density and microstructure of the

ceramics. The total conductivity of the material is therefore directly influenced by these aforementioned factors. Table 1 provides an overview of various processing conditions and reported conductivity values.

Powders with different characteristics are produced through different synthesis methods thus their sintering temperature is also different as listed in Table 1. This is due to different particle size, morphology and composition produced from different methods, evidencing a profound influence of synthesis methods on the processing temperature of ceramics (10).

Table 1: Various synthesis methods, processing parameters, and conductivities reported at room temperature for NASICONs.

| Method | | Conductivity at 25 °C ($mS\ cm^{-1}$) | Compaction pressure (MPa) | Sintering temperature (°C) | Sintering time (h) | Relative density (%) | Ref. |
|---|---|---|---|---|---|---|---|
| Solid-state reaction | | 0.75 | 300 | 1175 | 5, 24 | N/A | (12, 15-17) |
| | | 1.20 | 200 | 1275 | 25 | ~ 98 | |
| Solution-assisted solid-state reaction | | 1.00 | 150 | 1250 | 5 | ~ 93 | (10) |
| Sol–gel derived | Metal alkoxides | 0.60 | 100 | 1200 | 0.5 | ~ 70 | (18-23) |
| | Citrate gel (Pechini) | 0.86 | 150 | 1250 | 5 | ~ 91 | (10) |
| | Silica gel | 0.66 | N/A | 1200 | 48 | ~ 85-95 | (24-26) |
| Nonhydrolytic | | - | N/A | 1150-1200 | 15-20 | 92-95 | (27) |
| Coprecipitation | | 0.12 | 300 | 1175 | 5 | N/A | (11) |

In this study, we therefore systematically investigated the impact of sintering time and temperature by keeping the powder properties constant. To this end, pellets with a constant green density were sintered at 1200 °C and 1250 °C for 0 h, 2 h, 4 h, 6 h, 8 h, and 10 h each. The pellets obtained were studied by means of scanning electron microscopy and impedance spectroscopy to investigate the microstructural properties on bulk and grain boundary resistance.

## 2. Experimental

Nominal $Na_3Zr_2(SiO_4)_2(PO_4)$ was prepared by means of a solution-assisted solid-state reaction (SA-SSR) (10), whereby stoichiometric amounts of $NaNO_3$ (99.5 %), $ZrO(NO_3)_2$ (99 %), and $Si(OC_2H_5)_4$ (99 %), supplied from VWR International, Belgium, were mixed and dissolved in water using a quartz glass container. After the nitrates were dissolved in the solution, a stoichiometric amount of tetraethyl orthosilicate, $Si(OC_2H_5)_4$, was added. When the $Si(OC_2H_5)_4$ was hydrolyzed, a corresponding amount of $NH_4H_2PO_4$ was added and stirred for 30 minutes to form a homogeneous precipitation. The mixture was stirred overnight at 300 rpm and at a temperature of 50 °C. The homogenized mixture was initially heated from 50 °C up to 100 °C in order to slowly evaporate the water. The product was subsequently fired in a furnace at 600 °C for 3 h to form an amorphous raw powder. During heat treatment, the inorganic polymeric matrix was pyrolyzed and $NO_x$, $CO_2$, and $H_2O$ evolved as gaseous products. Afterwards, the raw powder was calcined at 800 °C for 12 h and ball-milled on a roller bench for 48 h using zirconia balls. The particle size distribution was obtained using Horiba LA-950V2 laser diffraction particle size distribution analyzer with ethanol as dispersing medium. The particle size of the milled powder was 2 µm. The milled powder was then pressed into pellets (diameter = 13 mm,

thickness = 1.1-1.2 mm) at a pressure of ~150 MPa. After pressing, all samples exhibited similar green densities, i.e. 59–61 % of theoretical density.

Green pellets were sintered at $T_s$ = 1200 °C and 1250 °C for $t_s$ = 0 h, 2 h, 4 h, 6 h, 8 h, and 10 h at a heating and cooling rate of 300 K/h. These temperatures were chosen because sintering at a higher temperature results in sample deformation due to partial melting. After sintering, the pellets were sputtered with gold as blocking electrodes. Electrical conductivity was measured using an impedance spectroscopy system (Biologic, VMP-300) between -30 °C and 100 °C in the frequency range of 1 Hz to 7 MHz.

The phase purity of the sintered specimens was measured by X-ray diffraction (XRD, Bruker D4 ENDEAVOR diffractometer with Cu $K_\alpha$ radiation), and the microstructure of the powder and pellet cross section were examined by scanning electron microscopy (SEM, ULTRA 55, ZEISS). Prior to microstructure investigation, the cross sections were polished and etched thermally at 1100 °C for 15 minutes. Microstructural details such as grain size distribution and fraction of porosity were determined using image analysis software (analySIS pro, Olympus Soft Imaging Solutions GmbH, Version 5.0). The density of the samples was measured using the Ultrapycnometer 1000, version 2.4 (Quantachrome Corporation), which uses gas displacement and the volume–pressure relationship (Boyle's law) to measure the relative density of the specimens.

The SEM images were analyzed using the analySIS pro imaging software, in which the grain boundary identification process is semi-automatic. It depends crucially on the discernibility of grain boundaries, which can be achieved by chemical or, in the case of our investigation, thermal etching. The SEM images were loaded into the program with suitable resolutions and calibrated. A "separator" command was subsequently used as a filter for separating objects (i.e. grains).

Using this filter, it is possible to separate segments of an image with different intensities, such as the interfaces of particles. The separator creates light or dark lines dividing objects of the same color or creates objects that are distinguishable from the background due to their intensity value. The software is also able to edit the resulting image interactively. Finally, statistical data of microstructural parameters are obtained. Since the grain size was obtained from 2D images, a multiplication factor of 1.571 was applied for tetrakaidecahedron-shaped particles in accordance with the ASTM standard (28).

Stoichiometry of the materials was controlled by means of inductively coupled plasma optical emission spectroscopy (ICP-OES) using the Thermo Scientific iCAP 7600 spectrometer with optical scale and CID semiconductor detector, axial and radial reflection, and wavelengths between 166 nm and 847 nm. 20 mg of powder was mixed to 0.25 g of lithium borate in a platinum crucible and heated for 0.5 h at 1000 °C. The liquefied material was dissolved in 30 mL of HCl (5%). After dissolution, the sample solutions were transferred to sample vials containing 0.5 mL of HF and filled to a volume of 50 mL. Each test sample was diluted and measured twice.

## 3. Results and discussion

### 3.1. X-ray diffraction

The XRD patterns were recorded to investigate the phase purity of NZSP after sintering at 1250 °C and at different times (Fig. 1). In all samples, monoclinic $ZrO_2$ was detected in addition to a well-crystallized monoclinic NASICON structure (space group C2/c). The amount of $ZrO_2$ was estimated to be 4 wt.% for $t_s$ = 4 h and 1 wt.% for $t_s$ = 0 h, whereas all other samples contained 2 wt.% $ZrO_2$. In addition, a very weak reflection at $2\theta = 28.06°$ might indicate the formation of

$SiO_2$. The samples sintered at 1200 °C for different times show similar crystallization trend and the presence of $ZrO_2$ as secondary phase.

The formation of $ZrO_2$ during the densification of $Na_3Zr_2(SiO_4)_2(PO_4)$ was also observed using other synthesis and processing methods (8, 11, 13). This is due to an earlier crystallization of $ZrO_2$ prior to NASICON formation, resulting from the high thermodynamic stability of $ZrO_2$ and not due to the volatility of reagents (e.g. sodium monoxide) at the sintering temperature. As demonstrated earlier, $ZrO_2$ starts to crystallize at 800 °C for SA-SSR powders (10). According to percolation theory, a small amount of $ZrO_2$ acts as porosity and has a minimal impact on $Na^+$ conduction. However, higher amounts of $ZrO_2$ might reduce the Zr content from the NASICON phase, thus resulting in stoichiometric differences that significantly influence bulk conductivity (2, 10).

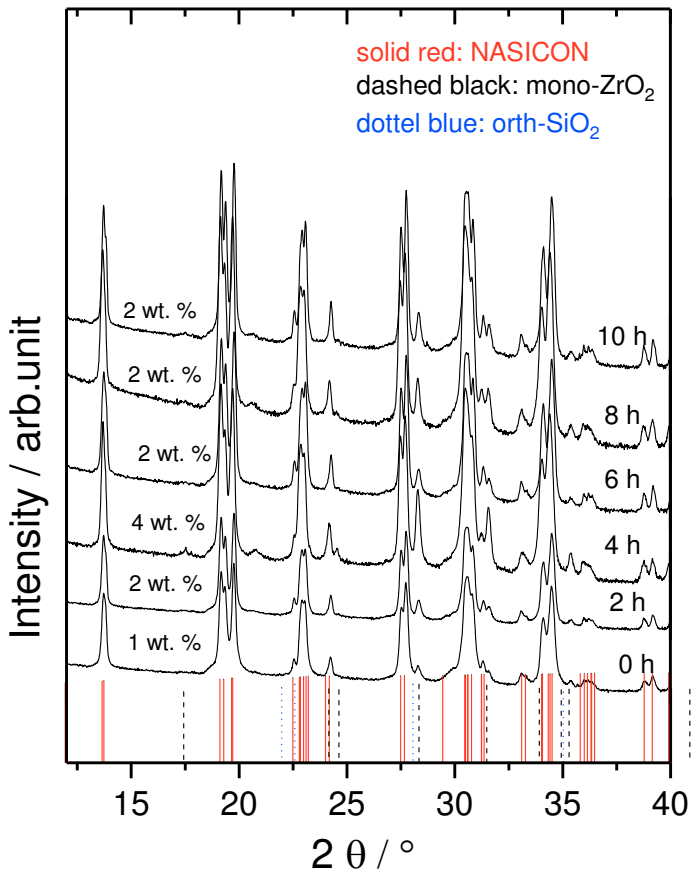

Fig. 1: The XRD patterns of NZSP sintered at 1250 °C for different dwell times. As a reference, the diffraction patterns of observed phases, i.e. $Na_3Zr_2Si_2PO_{12}$ (solid red line), monoclinic $ZrO_2$ (dashed black), and orthorhombic $SiO_2$ (dotted blue) (16, 29, 30) are also shown as vertical lines at the bottom of the graph. The percentage values denote the content of $ZrO_2$ in weight percent.

The chemical analysis of the NASICON materials (Fig. 2) revealed their respective stoichiometries. Overall, the stoichiometry lies within the expected range for all compositions with an experimental margin for error of ±3 %. However, a slight Na loss was observed in the pellets sintered at 1250 °C compared to those sintered at 1200 °C, which is due to the evaporation of sodium oxide. The contents of Zr and Si are similar at both $T_s$. Nevertheless, Zr was lower than expected in all samples.

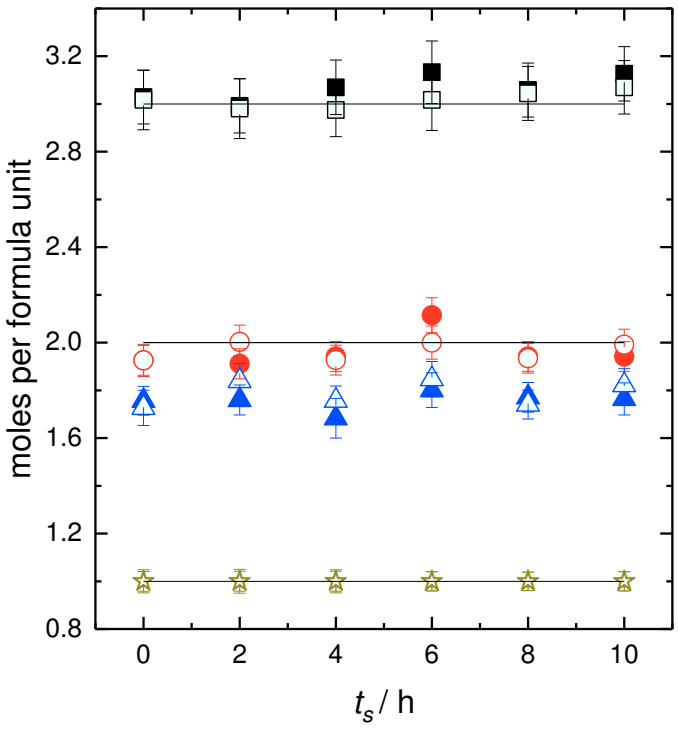


Fig. 2: Analytical stoichiometries obtained from ICP-OES. The filled and empty black squares (Na), red circles (Si), dark yellow stars (P), and blue triangles (Zr) represent samples sintered at

1200 °C and 1250 °C, respectively. The solid lines depict the nominal compositions and standard error including experimental error.

### 3.2.Microstructure

For $t_s$ = 1200 °C, the microstructure shows no densification for up to 2 h, after which it starts to densify and exhibit significant grain growth. Nonetheless, all the microstructures show substantial porosity (Fig. 4). At 1250 °C, however, the microstructure exhibits only minor densification for 0 h, i.e. just by heating the sample to maximum temperature. For sintering times of more than 2 h, the microstructure shows increasing densification and, hence, a linear increase in relative density in this density range, as seen in Fig. 3. Furthermore, gradual grain growth is also observed with an increase in sintering time for all the samples. Representative images of the microstructure of the pellets sintered at both temperatures for different sintering times are compiled in Fig. 4 and Fig. 5.

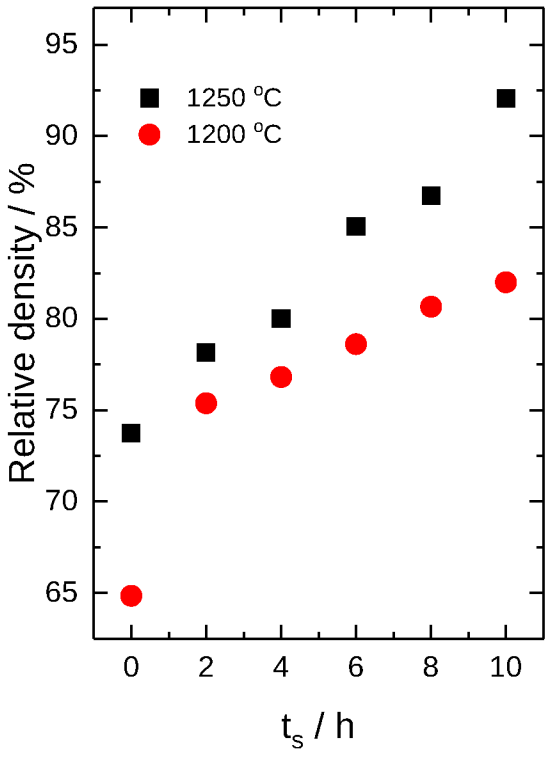


Fig. 3: The relative density of NZSP sintered at 1200 °C and 1250 °C measured by pycnometry.

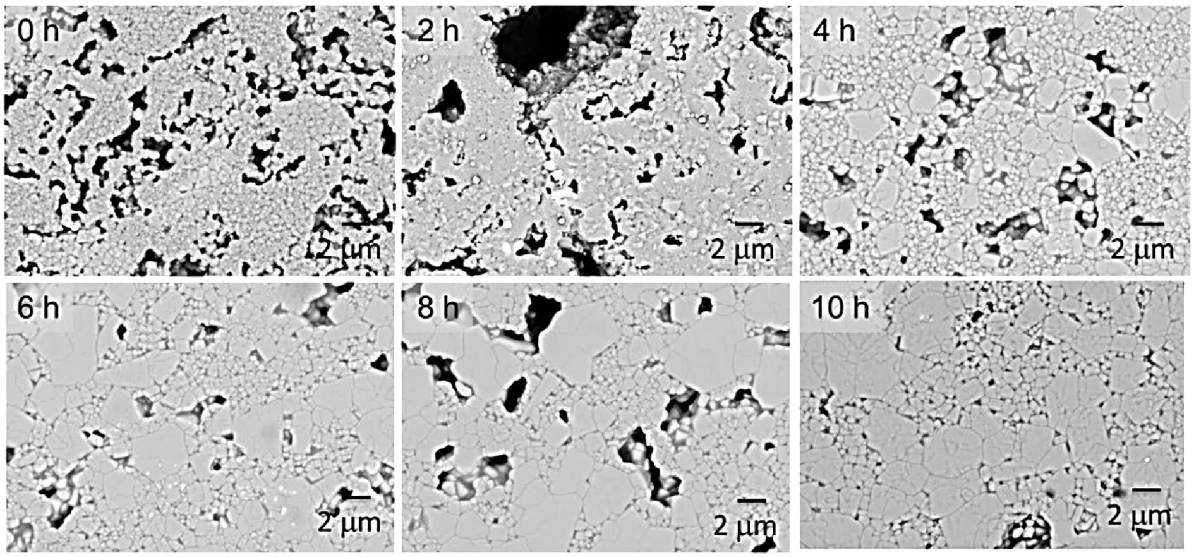


Fig. 4: SEM images of NZSP microstructure after sintering at 1200 ˚C for different dwell times.

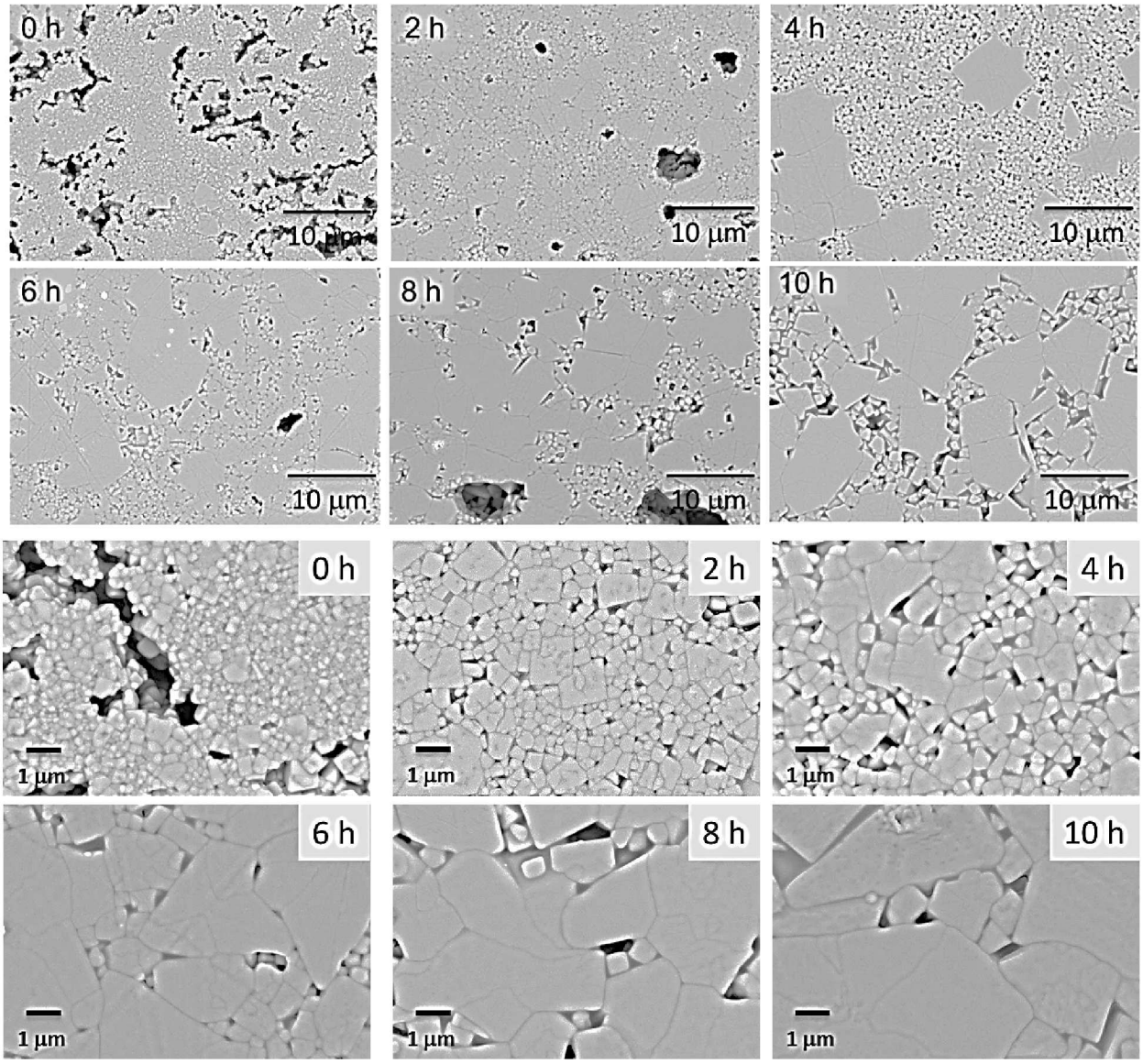


Fig. 5: Two sets of SEM images with different magnifications of an NZSP microstructure after sintering at 1250 ˚C for various dwell times. The two magnifications reveal a broader view of grain growth in two different size regimes.

Examples of SEM images analyzed using the analySIS pro imaging software are shown in Fig. 6 where the color categories reflect the different grain size intervals. The statistical data of microstructural parameters is given Table 2. The porosity obtained from image analysis is

smaller than pycnometric values because image analysis is performed only on a localized area whilst not take into account the artifacts such as voids and cracks.

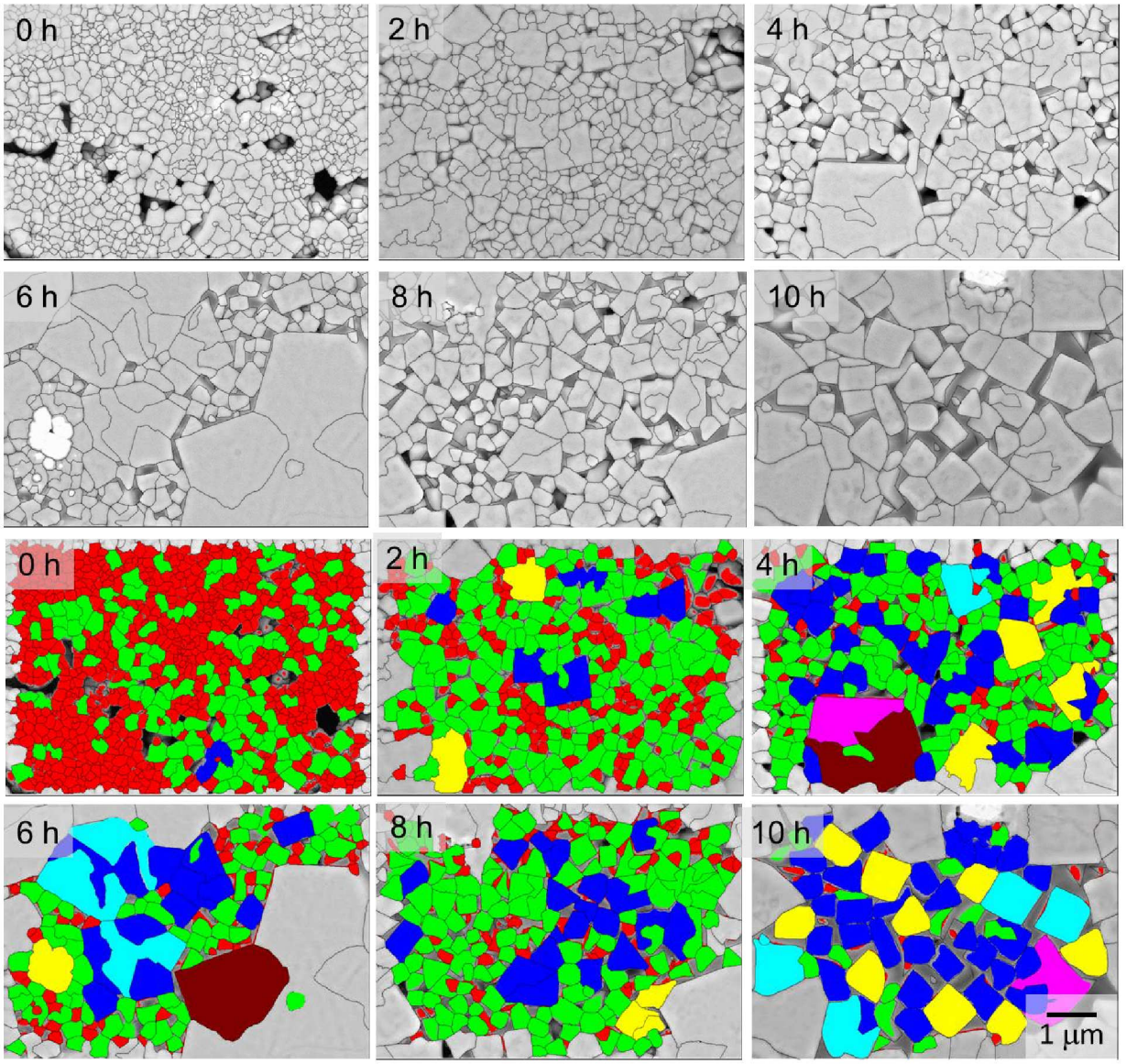


Fig. 6: Images of grain identification (upper two rows) and size statistics (lower two rows) using analySIS pro. The colors depict different intervals of grain sizes.

Table 2: The area fractions of different phases obtained by means of image analysis on samples sintered at 1250 °C.

| $t_s$ | Mean diameter (small) | Mean diameter (large) | NASICON | Glassy | Pores | $ZrO_2$ |
|---|---|---|---|---|---|---|
| h | μm | | Area % | | | |
| 0 | 0.645 ± 0.004 | - | 83.2 ± 1.5 | 1.7 ± 0.1 | 14.8 ± 1.5 | 0.1 ± 0.1 |
| 2 | 0.907 ± 0.008 | - | 92.7 ± 1.0 | 3.1 ± 0.3 | 3.6 ± 0.8 | 0.7 ± 0.4 |
| 4 | 1.032 ± 0.014 | 1.794 ± 0.060 | 91.9 ± 0.4 | 7.4 ± 0.3 | 0.8 ± 0.2 | 0.2 ± 0.0 |
| 6 | 1.139 ± 0.026 | 3.884 ± 0.173 | 92.0 ± 0.8 | 6.3 ± 0.6 | 1.0 ± 0.3 | 0.4 ± 0.1 |
| 8 | 1.319 ± 0.017 | 5.895 ± 0.173 | 92.4 ± 0.7 | 6.3 ± 0.6 | 1.0 ± 0.1 | 0.3 ± 0.1 |
| 10 | 1.763 ± 0.028 | 8.183 ± 0.047 | 91.1 ± 1.1 | 8.5 ± 1.0 | 0.4 ± 0.2 | 0.1 ± 0.1 |

The mean diameter is plotted as a function of relative density in Fig. 7a, revealing an abrupt increase of larger grains as compared to gradual increase of smaller grains. This abnormal grain growth can also be seen in Fig. 7b as a function of $t_s$. Possible reasons of abnormal grain growth are anisotropic grain boundary energy or high grain boundary mobility (31).

The grain size distributions indicate varying grain growth at different $T_s$ and $t_s$. At 1200 °C and up to 4 h, the grains were smaller than the threshold of picture analysis (0.5 μm). For longer times and a higher temperature, however, a systematic change in grain size distributions was observed. Evidently, grain growth is observed in all samples through a shift in the frequency distribution peaks towards larger diameters. In addition, the formation of a right shoulder indicates that grain growth occurs at multiple speeds within the samples. This phenomenon of abnormal grain growth is visible more clearly at 1250 °C (Fig. 8b), where a mono-modal distribution at 0 h transforms into a bi-modal distribution curve at 10 h, in addition to an overall

size increase of the initial grains (as seen in the SEM images). An abrupt increase in the grain size is observed after sintering at 1250 °C for more than 4 h in Fig. 7b, whilst for longer $t_s$ the grains grow further in two different sizes. This phenomenon of abrupt change in grain size and grain boundaries as a function of time and temperature can be conjointly represented in a time–temperature–transition (TTT) diagram (32, 33). However, this would require more experiments at different temperatures and dwell times in order to establish a complete TTT diagram for NASICONs.

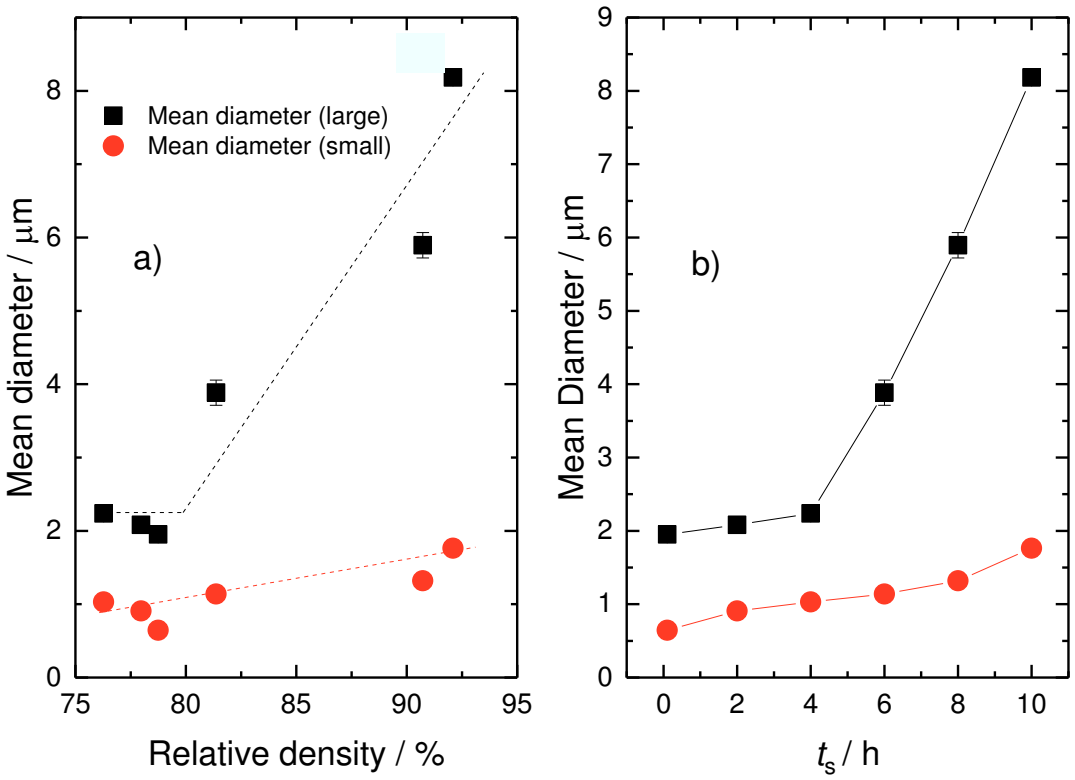


Fig. 7: a) Mean diameter as a function of relative density. b) Average grain size of initial and abruptly grown grains (only large grains were selected from Fig. 5). Both figures show data of samples sintered at 1250 °C.

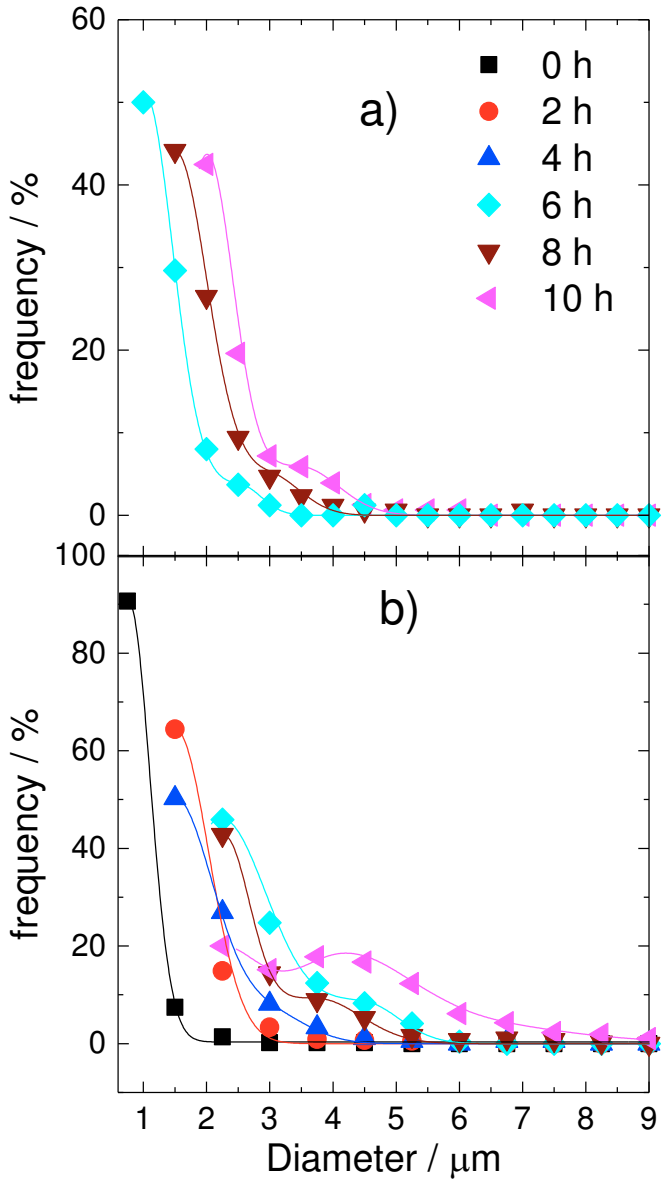


Fig. 8: The grain size distribution (normalized to the total number of particles) obtained from image analysis of specimens sintered at (a) 1200 °C and (b) 1250 °C. At 1200 °C, it was not possible to analyze the samples sintered for 0 h to 4 h due to their particle sizes being too small. For the particle diameters, a multiplication factor of 1.571 was applied for tetrakaidecahedron-shaped particles. The lines connecting the data points are drawn as a visual guide.

### 3.3.Electrical conductivity

The impedance spectra of samples sintered at both temperatures were measured from -30 °C to 100 °C, but only those obtained at -20 °C are shown in Fig. 9. For an accurate comparison, the impedance data were normalized to the dimensions of the pellets.

*3.3.1 Impedance spectra*

The complex impedance plot of the samples sintered at 1200 °C and 1250 °C for different dwell times is shown in Fig. 9. The impedance spectra comprise two semicircles, each corresponding to the contribution of a certain process (bulk or grain boundary) and, as a whole, result in the total impedance. The semicircle visible at a higher frequency, generally referred to as the first semicircle, represents the contribution of the material's bulk resistance. The first semicircle is the intrinsic property of a material and mainly depends on its composition. The second semicircle appearing at a lower frequency arises from the grain boundary contribution to the total impedance. This semicircle is the property of an extrinsic material and depends on the processing conditions and characteristics of the starting powder.

In Fig. 9, the impedance spectra are normalized to the sample dimensions and thus allow a direct comparison of the spectra. The base material is the same for all samples ($Na_3Zr_2Si_2PO_{12}$), differing only in terms of sintering conditions. It can therefore be assumed that the bulk impedance of the samples should not differ much. However, the grain boundary impedance may differ substantially. This is a result of the increased densification and grain growth due to the higher sintering temperature and prolonged dwell time, respectively, resulting in turn in the alteration of the transport processes across grain boundaries. The sample sintered at 1250 °C for

10 h (Fig. 9b) has the lowest grain boundary resistance due to its larger grain sizes compared to the other samples.

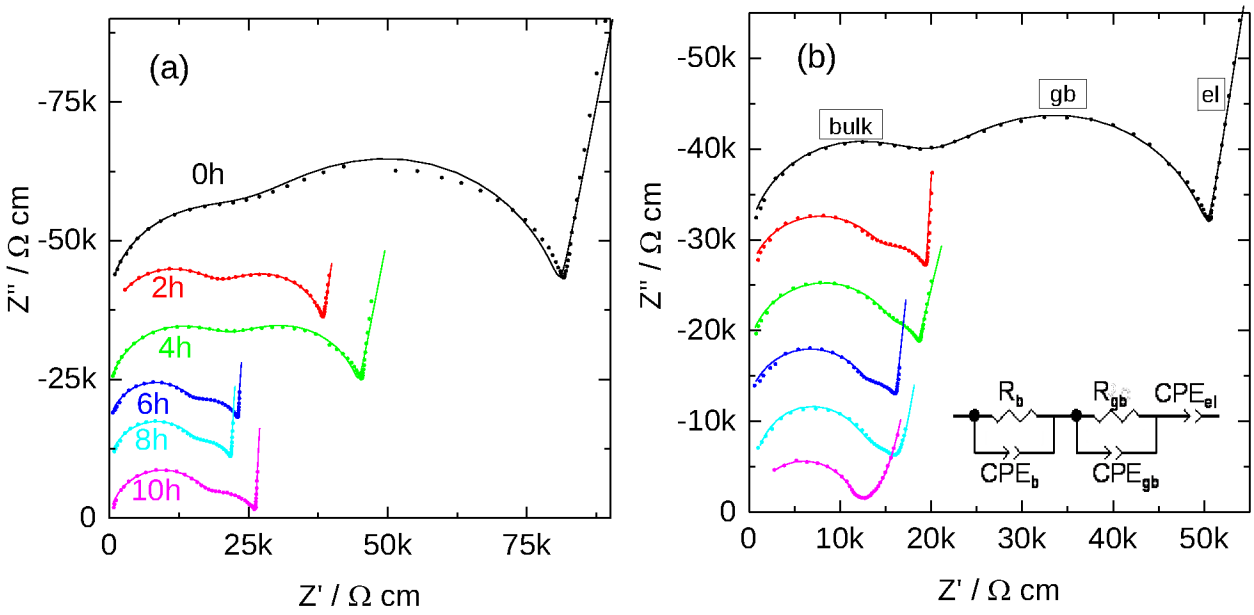


Fig. 9: Impedance spectra (at -20 °C) of NZSP sintered at (a) 1200 °C and (b) 1250 °C for different sintering times. Dotted and solid lines depict experimental and fitting data, respectively.

*3.3.2 Electrical conductivity*

The total conductivity as well as the conductivity of the bulk ($\sigma_b$) and grain boundaries ($\sigma_{gb}$) can be obtained by fitting the impedance spectra with an equivalent circuit (see Fig. 9). At -20 °C, the resistances represent the ionic conductive paths in the bulk, i.e. within the particles, ($R_b$) and across the grain boundaries ($R_{gb}$). For both sets of samples, the resistances are obtained by fitting the impedance spectra and extracting the lowest value of –Z'' as the total resistance. The constant phase elements (CPE) represent the non-ideal capacitive contributions of the transport processes in the bulk ($CPE_b$), at the grain boundaries ($CPE_{gb}$), and at the electrode/electrolyte interface at low frequencies ($CPE_{el}$). The CPE is defined by a capacity value, $C_{CPE}$, and an exponent, *n* (see

Eq. (1)). If *n* equals 1, then the equation is identical to that of a capacitor. If *n* equals 0.5, a 45 degree line is produced on the complex plane graph. When a CPE is placed in parallel to a resistor, a Cole element (depressed semi-circle) is produced. The obtained fitting data are given in Table 3. In the software used to analyze the impedance spectra (Zview®), the CPEs can be used to simulate the imperfect capacitance of transport processes. The impedance of the CPE is calculated using Eq. (1) with ω as the frequency. The exponent *n* usually varies between 1 and 0.5. The $C_{CPE}$ is related to the capacitance C as written in Eq. (2) (34).

$$Z_{CPE} = \frac{1}{C_{CPE}(j\omega)^n} \quad (1)$$

$$C = R^{\frac{1-n}{n}} C_{CPE}^{1/n} \quad (2)$$

When $n \rightarrow 1$ then $C_{CPE} \rightarrow C$ and an ideal capacitor is observed, whilst decreasing *n* indicates a non-ideal system, e.g. when $n = 0.5$ then a pure diffusion process is involved. The capacitance associated with the high-frequency arc is found to be around $10^{-11}$ F and the one associated to the lower frequency arc lies between $10^{-9}$ and $10^{-8}$ F. The high-frequency arc can therefore be identified as a bulk property due to the fact that its capacitance is in the pF order, whereas the lower frequency arc can be identified as the grain boundary resistance since its capacitance is in the nF range. The third capacitance represented by $CPE_{el}$ is found to be of the μF order and is associated with the polarization of the electrode (34).

Table 3: Fitting data of impedance spectra at -20 °C shown in Fig. 9.

| $t_s$ | $R_b$ (Ω cm) | $R_{gb}$ (Ω cm) | $C_b$ (F) | $n_b$ | $C_{gb}$ (F) | $n_{gb}$ | $C_{el}$ (F) | $n_{el}$ | *Sum of Sq. error |
|---|---|---|---|---|---|---|---|---|---|
| **$T_s$ = 1200 °C** | | | | | | | | | |
| 0h | 2.30E+04 | 5.82E+04 | 6.98E-11 | 0.95 | 4.64E-10 | 0.85 | 1.26E-06 | 0.89 | 0.13 |
| 2h | 1.94E+04 | 1.89E+04 | 7.00E-11 | 0.93 | 1.64E-09 | 0.89 | 2.74E-06 | 0.91 | 0.08 |
| 4h | 2.08E+04 | 2.41E+04 | 8.50E-11 | 0.95 | 1.21E-09 | 0.89 | 1.12E-06 | 0.90 | 0.06 |
| 6h | 1.53E+04 | 7.67E+03 | 8.53E-11 | 0.95 | 3.66E-09 | 0.91 | 9.43E-07 | 0.96 | 0.44 |
| 8h | 1.60E+04 | 5.65E+03 | 8.38E-11 | 0.93 | 5.00E-09 | 0.95 | 7.67E-07 | 0.96 | 0.56 |
| 10h | 1.74E+04 | 8.79E+03 | 8.10E-11 | 0.96 | 3.68E-09 | 0.85 | 6.47E-07 | 0.97 | 0.72 |
| **$T_s$ = 1250 °C** | | | | | | | | | |
| 0h | 1.94E+04 | 3.05E+04 | 8.08E-11 | 0.95 | 1.26E-09 | 0.88 | 1.82E-06 | 0.90 | 0.71 |
| 2h | 1.51E+04 | 4.29E+03 | 8.78E-11 | 0.90 | 6.84E-09 | 0.99 | 4.93E-07 | 0.97 | 0.68 |
| 4h | 1.62E+04 | 2.00E+03 | 9.27E-11 | 0.92 | 1.23E-08 | 0.98 | 8.06E-07 | 0.83 | 0.80 |
| 6h | 1.32E+04 | 2.80E+03 | 9.51E-11 | 0.93 | 1.18E-08 | 0.98 | 5.34E-07 | 0.93 | 0.58 |
| 8h | 1.42E+04 | 2.82E+03 | 7.98E-11 | 0.93 | 1.20E-08 | 0.77 | 3.54E-07 | 0.89 | 0.20 |
| 10h | 1.17E+04 | 2.68E+03 | 8.55E-11 | 0.96 | 2.60E-08 | 0.78 | 1.46E-07 | 0.87 | 0.07 |

*it is proportional to the average percentage error between the original data points and the calculated values

The bulk and grain boundary conductivities can be extracted from the impedance diagrams using the brick layer model (35, 36). According to this model, the real grain boundary conductivity ($\sigma_{gb,real}$) is often incorrectly reported in the literature. Whereas $\sigma_b$ can be calculated with

$$\sigma_b = \frac{L}{AR_b} \tag{3}$$

and normalized to the sample dimensions, the analogue calculation of $\sigma_{gb,norm}$ using Eq. 4

$$\sigma_{gb,norm} = \frac{L}{AR_{gb}} \tag{4}$$

is often misinterpreted as the "real" $\sigma_{gb,real}$. This way of calculating $\sigma_{gb}$ is not correct because the actual volume fraction of the grain boundaries is much smaller than the volume fraction of grains within the sample dimensions. Therefore, the $\sigma_{gb,real}$ has to be calculated taking into account the net contribution of grain boundaries in the total conductivity using Eq. 5 with the capacitance obtained from Eq. 2.

$$\sigma_{gb,real} = \frac{L}{A}\left(\frac{C_b}{C_{gb}}\right)\frac{1}{R_{gb}} \tag{5}$$

Here $R_{gb}$ is the grain boundary resistance, $L$ is the thickness of sintered pellets, and $A$ is the area of the electrodes. Hence, $\sigma_{gb,real}$ is obtained using the ratio of the capacitances of bulk and grain boundaries and represents the real conductivity of the grain boundaries. The ratio $C_b/C_{gb}$ is the overall volume fraction of grain boundaries in the sample, assuming that both bulk and grain boundaries have the same dielectric constants (34).

The $\sigma_b$, $\sigma_{gb,real}$, and $\sigma_{gb,norm}$ are calculated using Eq. 3–5 and are shown in Fig. 10. The $\sigma_b$ (black lines) increases very slightly when the sintering time is increased due to grain growth and improving crystallization, which results in less resistance to mobile charge carriers. The $\sigma_{gb,real}$ (red lines) is about one order of magnitude smaller than $\sigma_b$ and does not change substantially after sintering at 1200 °C. However, it decreases significantly for a prolonged dwell time at 1250 °C. This deviation is due to changes in the transport properties across the grain boundaries, which arise from multiple processes, such as grain boundary diffusion and grain boundary complexions (32, 33).

The $\sigma_{gb,norm}$ (blue line) increases with increasing $t_s$ for both temperatures. Although the $\sigma_{gb,norm}$ is conventionally regarded as $\sigma_{gb}$, any interpretation in terms of microstructure would be misleading because $\sigma_{gb,norm}$ is calculated by normalizing the $R_{gb}$ to the whole sample dimensions and not to the grain boundary dimensions itself. Therefore, based on the higher values of $\sigma_{gb,norm}$, it would be incorrect to conclude that ionic transport is favorable and governed along grain boundaries. Nevertheless, it would be correct to compare $R_{gb}$ in terms of microstructural changes, since it represents the overall resistance induced by the grain boundaries to $Na^+$ conduction. For instance, in Fig. 9, it appears at first glance as if the grain boundary resistivity is lower than that of the bulk, particularly for samples sintered for 8 h or 10 h. Upon closer examination of these materials, the samples reveal larger grains (see Fig. 3) and exhibit a lower grain boundary resistance simply because fewer boundaries are encountered by the mobile charge carriers. These results are coherent with proton-conducting $BaCe_{0.85}Gd_{0.15}O_{2.975}$, where a reduction in $R_{gb}$ was also observed by increasing the grain size (34).

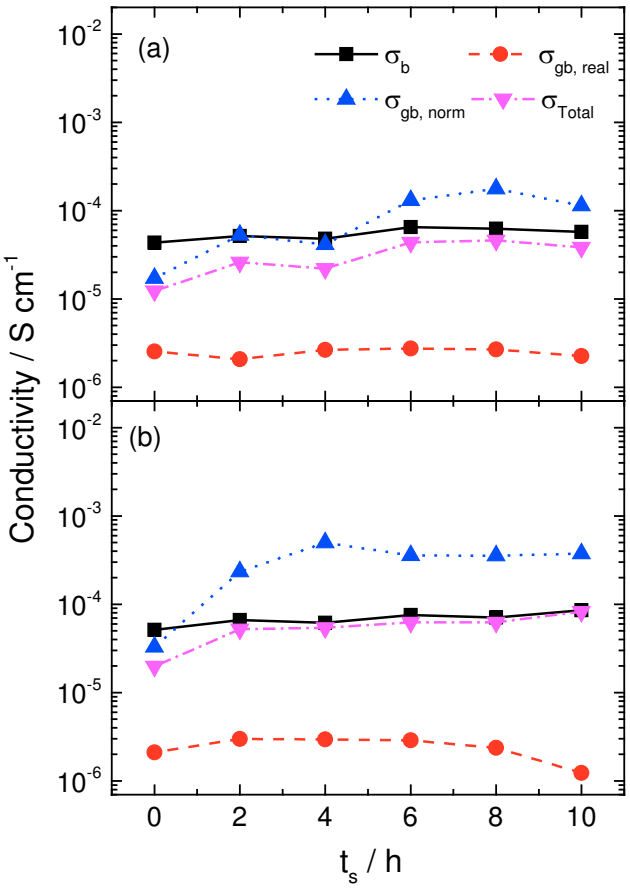


Fig. 10: Conductivity contributions as a function of dwell time after sintering at (a) 1200 °C and (b) 1250 °C. The measurements were performed at -20 °C.

A correlation between conductivity and density is shown in Fig. 11 including data from previous studies. Conductivity rises by almost one order of magnitude by increasing the relative density from 65 % to 93 %, which underlines the importance of sintering conditions in ceramic technology. The generalized effective media theory (GEM) (37) is often applied to simulate the transport properties of multi-phase materials. This model was developed only for composites with specific microstructures and is very valuable for cermets and semiconducting ceramics, but it does not take into account detailed microstructural features such as grain size, grain anisotropy,

and orientation. It is therefore not surprising that the GEM curve in Fig. 11 does not fit the data very well. The formula used

$$\sigma = \sigma_{ic}^{0}\left(1 - \frac{V_p + V_{ZrO2}}{V_{iso,c}}\right)^{n} \quad (6)$$

(with $\sigma_{ic}^{0}$ as the specific conductivity of the ionic conductor, $V_p$ and $V_{ZrO2}$ the volume fraction of pores and zirconia, respectively, $V_{iso,c}$ the critical volume fraction of isolating phases, where the first percolation pathways are formed by the ionic conductor, and $n$ as an empirical exponent) does not include the grain boundary contributions. Therefore, several models have been developed for solid electrolytes in combination with the brick-layer model (38, 39). In its simplest form, the GEM formula can be expanded by taking into account the volume of grain boundaries and grain boundary conductivity. Since $C_b/C_{gb}$ is regarded as the volume fraction of grain boundaries, which depends on the densification of the samples (as listed in Table 3), and the grain boundary conductivity can be assumed as constant ($\sigma_{gb,real}$ = 2 – 4 x $10^{-6}$ S/cm$^{-1}$, see Fig. 10), the GEM formula can be extended by the rule of mixtures to

$$\sigma = \left(\sigma_{ic}^{0}\left(1 - V_{iso} - V_{gb}\right) + V_{gb}\sigma_{gb}\right)\left(1 - \frac{V_{iso}}{V_{iso,c}}\right)^{n} \quad (7)$$

Where $V_{iso} = V_p + V_{ZrO2}$, and an exponential decay can be used to fit the dependence of the grain boundary volume fraction on density according to

$$V_{gb} = C_b/C_{gb} = 96.93\, e^{(-V_{ic}/0.10364)} - 0.0134 \quad (8)$$

The resulting curve agrees much better with the observed data (dashed line in Fig. 11).

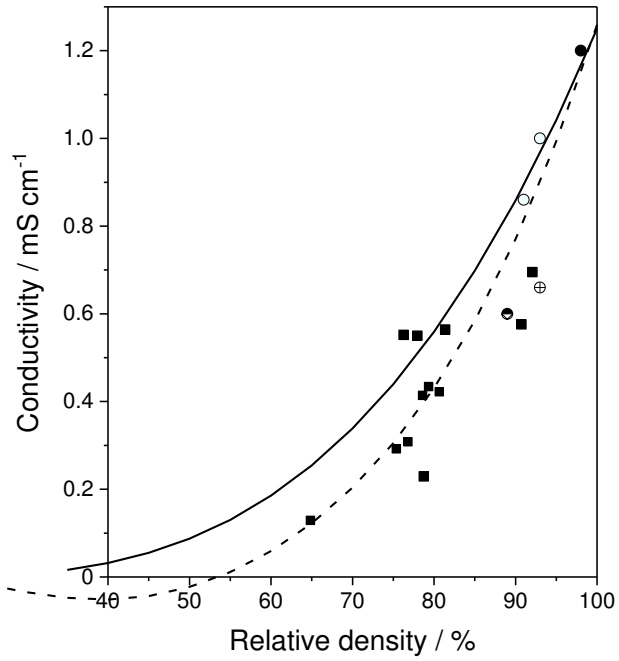


Fig. 11: Correlation of the relative density and total conductivity of NZSP samples (filled squares). Conductivity measurements were performed at room temperature (25 °C). Additional data were taken from refs. (18) (half-filled circle), (24) (crossed circle), (10) (open circles), (12) (filled circle). The GEM curve (eq. 6, solid line) and modified GEM curve (eq. 7, dashed line) was calculated with $\boldsymbol{\sigma_{ic}^{0}}$ = 1.25 mS cm$^{-1}$, $V_{iso,c}$ = 0.85 and $n$ = 3.

*3.3.3 Activation energies*

The total conductivity ($\sigma_{total}$) was calculated from the sum of $R_b$ and $R_{gb}$ of the samples and is plotted as a function of inverse temperature in Fig. 12. $\sigma_{total}$ follows the Arrhenius law and the activation energies (Table 4) were calculated from the slope of the straight line in a ln($\sigma$·T) vs. 1/T plot.

In Fig. 12a, conductivity deviates slightly from the Arrhenius behavior at temperatures ~ 90 °C. This is not observed for samples sintered at 1250 °C. This phenomenon is assumed to be a result

of the absorption of water molecules in the samples with higher porosity, which are desorbed at a higher temperature and thus cause this deviation (40).

After sintering at 1250 °C, all lines overlap at room temperature, except for 0 h, indicating no significant difference in $\sigma_{total}$. The activation energy ($E_{a,\ total}$) however decreases with the increasing sintering time and agrees with the observed grain growth in the microstructure. The grain growth densifies the sample by reducing the net amount of porosity as well as the net amount of grain boundary area. E.g. lower activation energy for longer sintering times indicates that the increase in grain size reduces the net amount of grain boundary area and consequently the $R_{gb}$. Therefore, the resistance of $Na^+$ hopping decreases as the ions incur reduced grain boundaries due to grain growth at longer sintering times (Fig. 2 and section 3.1). For a better understanding of the process, grain and grain boundary conductivities are plotted separately in Fig. 13.

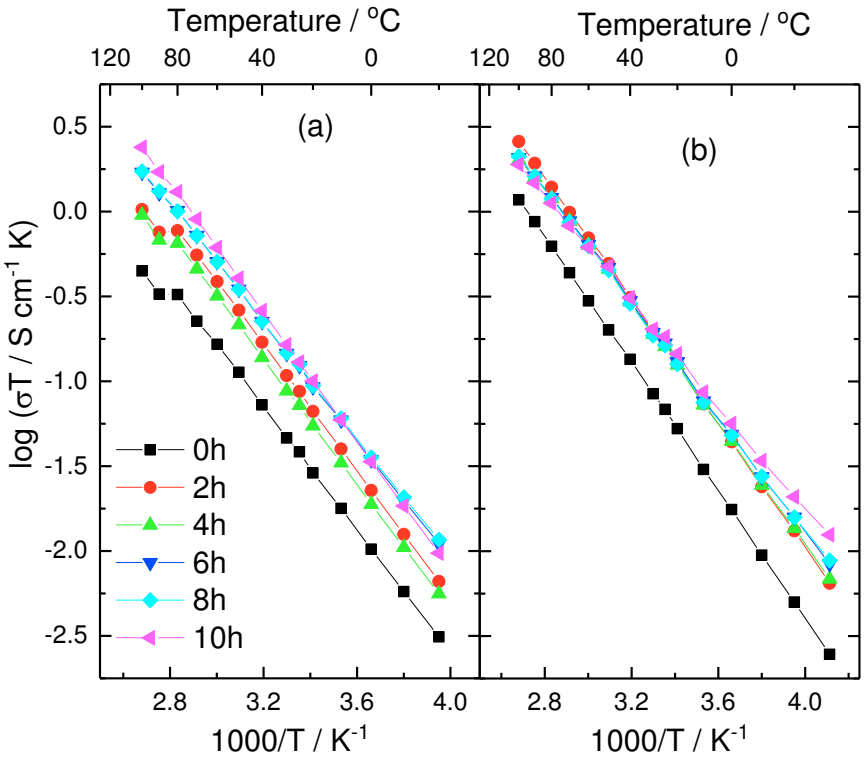


Fig. 12: Arrhenius-type plot of the total conductivity of NZSP sintered at (a) 1200 °C and (b) 1250 °C for different sintering times.

Table 4: Activation energies of $\sigma_{total}$ derived from a ln(σT) vs. 1/T plot according to Fig. 12.

| $t_s$ / h | $T_s$ = 1200 °C | $T_s$ = 1250 °C |
|---|---|---|
| 0 | 0.339 ± 0.006 | 0.372 ± 0.001 |
| 2 | 0.350 ± 0.006 | 0.361 ± 0.001 |
| 4 | 0.349 ± 0.005 | 0.345 ± 0.003 |
| 6 | 0.335 ± 0.005 | 0.334 ± 0.002 |
| 8 | 0.331 ± 0.006 | 0.333 ± 0.002 |
| 10 | 0.374 ± 0.001 | 0.307 ± 0.002 |

Two semicircles were only observed up to 0 °C and 10 °C for samples sintered at 1200 °C and 1250 °C, respectively. Both the $\sigma_{gb,real}$ and $\sigma_{gb,norm}$ are calculated using Eq. 4 and Eq. 5. It is important to remark that at 0 °C, obtaining $\sigma_{gb,real}$ becomes unreliable for 1250 °C sintered samples when $t_s$ > 6 h, due to very low $n$ values (< 0.5; Eq. 2). However for 1200 °C sintered samples even for longer $t_s$ the $n$ values are > 0.9 and the calculations were reasonable since the $\sigma_{gb,real}$ calculation assumes that the dielectric coefficient of grain boundaries remain equal to the bulk and effects only the magnitude of the conductivity. Therefore, the $E_a$ values obtained from an Arrhenius plot of $\sigma_{gb,norm}$ are used even though the magnitude of the conductivity is incorrect. It also illustrates why $\sigma_{gb,norm}$ is widely adopted as $\sigma_{gb,real}$, given that $\sigma_{gb,real}$ calculation is possible only for materials and at temperatures where grain boundary resistance contributes significantly to the total resistance.

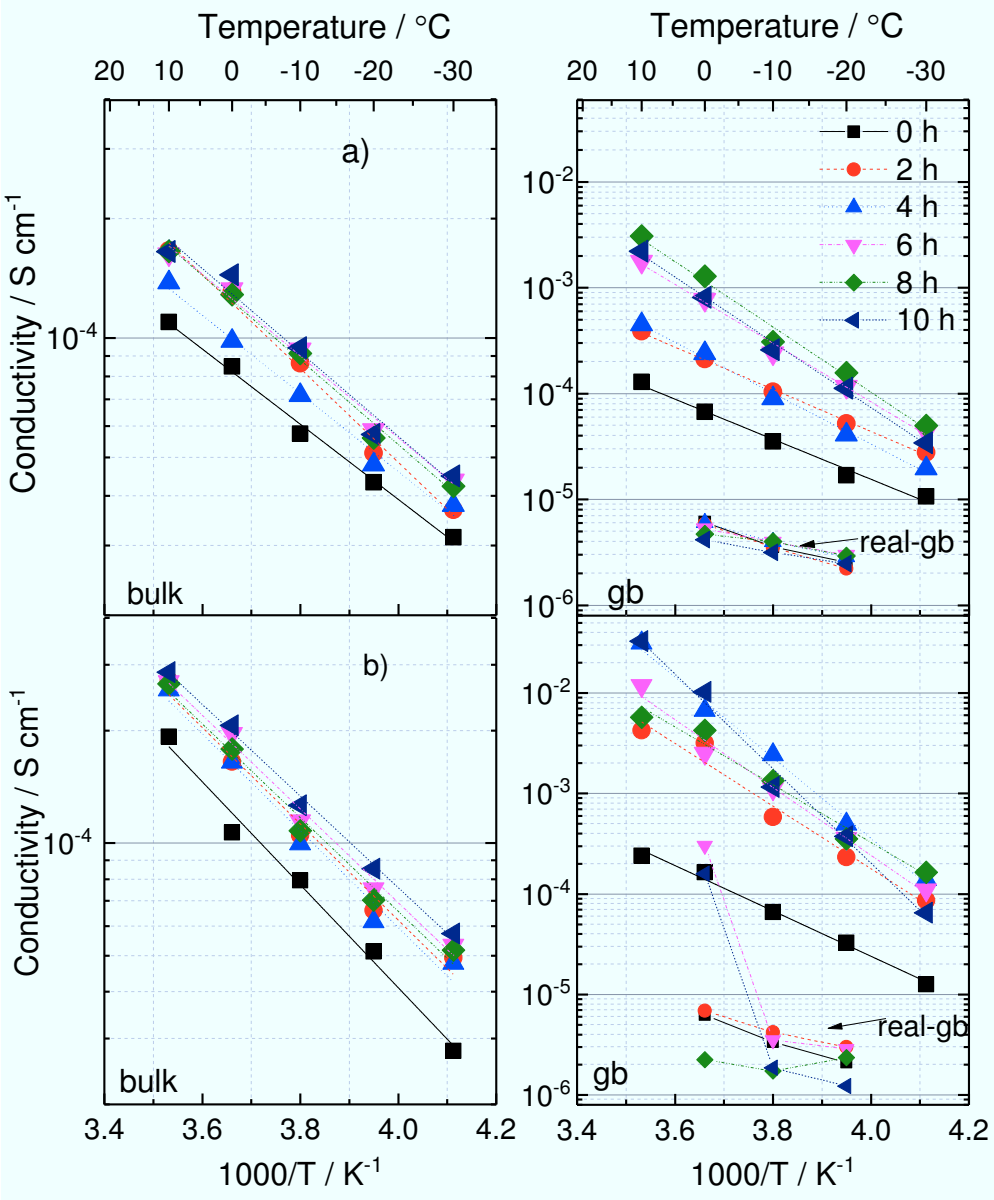


Fig. 13: Arrhenius-type plots of $\sigma_b$ and $\sigma_{gb}$ as well as $\sigma_{gb,real}$ obtained in the temperature range from -20 to 10 °C of samples sintered at (a) 1200 °C and (b) 1250 °C.

The obtained activation energies of each process are shown in Fig. 13. The values of $E_{a,b}$ are nearly constant for the two different sintering temperatures, varying between 0.21 and 0.28 eV. However, the $E_{a,gb}$ values are significantly increasing with dwell time. After sintering at 1200 °C $E_{a,gb}$ systematically increases from 0.35 to 0.59 eV, which indicates a systematic alteration of the

transport properties at the grain boundaries, which are affected only by the dwell time. The grain growth and small changes in stoichiometry due to evaporation of sodium oxide could be the only processes happening during sintering. However, after sintering at higher temperature (1250 °C), the $E_{a,gb}$ follows an irregular trend showing fluctuating transport properties across the grain boundaries by increasing the dwell time with an overall increase from 0.42 to 0.97 eV. The non-uniform $E_{a,gb}$ trend is an indication that multiple processes are affecting the grain boundary chemistry. These processes, in addition to obvious grain growth starting at $t_s$ = 4 h and presumably reducing the activation energy, could be a simultaneous increase of the glassy phase. Since the amount of this phase is substantially increasing from $t_s$ = 8 h to $t_s$ = 10 h, it is likely that the increasing volume fraction of this phase might be associated with the strong increase of $E_{a,gb}$. This is confirmed by a correlation between the glassy-phase obtained from image analysis and $E_{a,\ gb}$, both giving similar trends as shown by dotted line connecting the steric symbols in Fig. 14b. It can be noticed, however, that despite fluctuations in $E_{a,gb}$ values they only have a minor impact on the total conductivity.

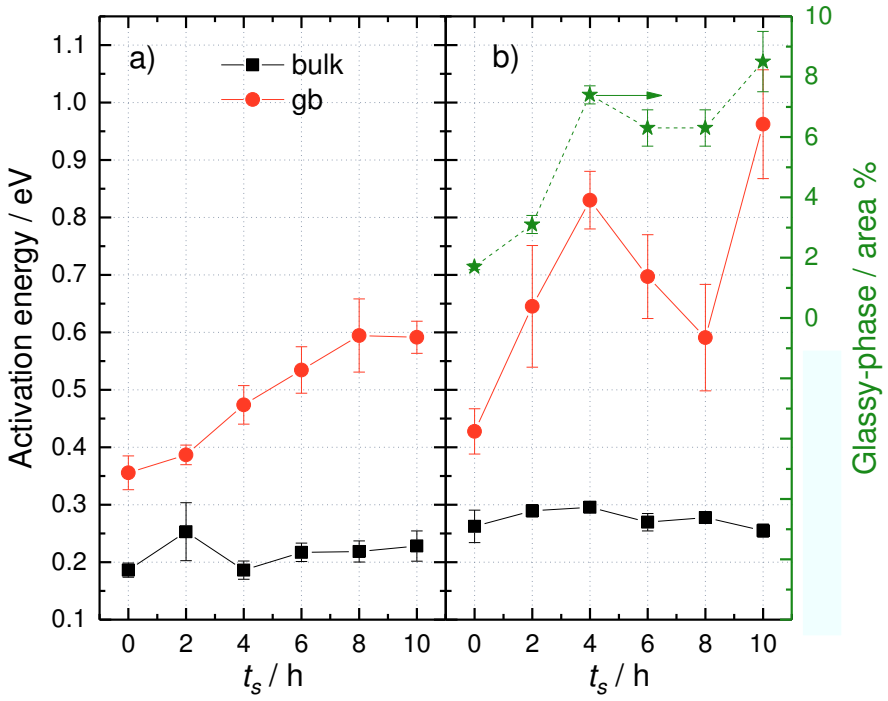


Fig. 14: Activation energies of the bulk and grain boundary conductivities of samples sintered at (a) 1200 °C and (b) 1250 °C. The Ea's are obtained from Arrhenius equation according and are in agreement with for NZSiP composition (41, 42). A correlation with the percentage of glass phase is also included from Table 2.

In a previous work, Fuentes et al. (43) conducted a similar study on a different NASICON material ($Na_3Y_{0.12}Zr_{1.88}Si_2PO_{12}$) and found that the impact of sintering temperature ($T_s$) was negligible on the $E_a$ values. However, by increasing the sintering time ($t_s$), they observed a decreasing $E_a$, which is in agreement with our study. Their sample sintered at 1220 °C for 80 h had an $E_a$ of 0.26 eV, which is similar to the $E_a$ of bulk conductivity of NZSiP. Assuming a negligible impact of the Y substitution, this evidence can be used to support the argument that

prolonged sintering ($t_s$ = 80 h) would result in large grain growth and decreasing grain boundary resistance. For the extreme situations of $t_s$ this leads to the limits

$$\lim_{t_s \to 0} \; E_a \; \to E_{a,gb} \;\; and \;\; \sigma \; \to \sigma_{gb}$$

$$\lim_{t_s \to \infty} \; E_a \; \to E_{a,b} \;\; and \;\; \sigma \; \to \sigma_{b}$$

## 4. Conclusions

The conductivity of NASICON materials is dependent on processing conditions and synthesis. The heat treatment or sintering conditions control the microstructure. Grain and grain boundary resistance can be controlled by tuning the microstructure. Sintering at higher temperature leads to a better densification, whilst prolonging the sintering time leads to grain growth. Higher densification and larger grains result in smaller grain boundary resistance and, as a consequence, high conductance. The recommended sintering conditions are 1250 °C for 10 h in air, starting with a green density of ~ 60 %. The activation energy data show that sodium ion conduction through the bulk is easier than through the grain boundaries. The activation energy of grain boundary conductivity is higher at a sintering temperature of 1250 °C than at 1200 °C. Because the net amount of grain boundary area is very low compared to bulk surface, the influence of grain boundary conductivity on the total conductivity is so low that it is unnoticeable in the Arrhenius plots. Grain boundary complexion is affected by both sintering time and temperature. A systematic study of more sintering time and temperature would allow develop a time-

temperature-transition diagram, which would allow obtaining a predictable microstructure by implementing the knowledge of grain boundary complexions.

**Acknowledgments**

The authors thank Dr. Y. J. Sohn and Ms. S. Schwartz-Lückge for Rietveld refinements of the XRD measurements and ultrapycometer investigations, respectively. The authors would also like to thank colleagues at ZEA-3 (Forschungszentrum Jülich) for carrying out the ICP-OES measurements. We are also grateful for financial support from the Ministry of Innovation, Science and Research of the State of North Rhine-Westphalia in terms of the starting funds for Helmholtz Institute Münster (Az. 433).

## References


1. Vogel EM, Cava RJ, Rietman E. $Na^+$ ion conductivity and crystallographic cell characterization in the Hf-nasicon system $Na_{1+x}Hf_2Si_xP_{3-x}O_{12}$. Solid State Ionics. 1984;14(1):1-6.
2. von Alpen U, Bell MF, Höfer HH. Compositional dependence of the electrochemical and structural parameters in the Nasicon system ($Na_{1+x}Si_xZr_2P_{3-x}O_{12}$). Solid State Ionics. 1981;3-4(C):215-8.
3. Fuentes RO, Figueiredo FM, Soares MR, Marques FMB. Submicrometric NASICON ceramics with improved electrical conductivity obtained from mechanically activated precursors. Journal of the European Ceramic Society. 2005;25(4):455-62.
4. Song SF, Duong HM, Korsunsky AM, Hu N, Lu L. A $Na^+$ Superionic Conductor for Room-Temperature Sodium Batteries. Scientific Reports. 2016;6.
5. Ma Q, Guin M, Naqash S, Tsai CL, Tietz F, Guillon O. Scandium-Substituted $Na_3Zr_2(SiO_4)_2(PO_4)$ Prepared by a Solution Assisted Solid-State Reaction Method as Sodium-Ion Conductors. Chemistry of Materials. 2016;28(13):4821-8.
6. Abraham KM, Elliot JE. moderate temperature sodium cells. 5. discharge reactions and rechargeability of NiS and $NIS_2$ positive electrodes in molten $NaAlCl_4$. Journal of the Electrochemical Society. 1984;131(10):2211-7.
7. Noguchi Y, Kobayashi E, Plashnitsa LS, Okada S, Yamaki J-i. Fabrication and performances of all solid-state symmetric sodium battery based on NASICON-related compounds. Electrochimica Acta. 2013;101:59-65.
8. Lalère F, Leriche JB, Courty M, Boulineau S, Viallet V, Masquelier C, et al. An all-solid state NASICON sodium battery operating at 200°C. Journal of Power Sources. 2014;247:975-80.
9. Kim J, Jo SH, Bhavaraju S, Eccleston A, Kang SO. Low temperature performance of sodium–nickel chloride batteries with NaSICON solid electrolyte. Journal of Electroanalytical Chemistry. 2015;759(Part 2):201-6.
10. Naqash S, Ma Q, Tietz F, Guillon O. $Na_3Zr_2(SiO_4)_2(PO_4)$ prepared by a solution-assisted solid state reaction. Solid State Ionics. 2017;302:83-91.
11. Ignaszak A, Pasierb P, Gajerski R, Komornicki S. Synthesis and properties of Nasicon-type materials. Thermochimica Acta. 2005;426(1–2):7-14.
12. Hayashi K, Shima K, Sugiyama F. A mixed aqueous/aprotic sodium/air cell using a NASICON ceramic separator. Journal of the Electrochemical Society. 2013;160(9):A1467-A72.
13. Lee JS, Chang CM, Lee YI, Lee JH, Hong SH. Spark Plasma Sintering (SPS) of NASICON Ceramics. Journal of the American Ceramic Society. 2004;87(2):305-7.
14. Anantharamulu N, Koteswara Rao K, Rambabu G, Vijaya Kumar B, Radha V, Vithal M. A wide-ranging review on Nasicon type materials. Journal of Materials Science. 2011;46(9):2821-37.
15. Takahashi T, Kuwabara K, Shibata M. Conductivities of $Na^+$ ion conductors based on NASICON. Solid State Ionics. 1980;1(3–4):163-75.
16. Hong HYP. Crystal structures and crystal chemistry in the system $Na_{1+x}Zr_2Si_xP_{3-x}O_{12}$. Materials Research Bulletin. 1976;11(2):173-82.
17. Goodenough JB, Hong HYP, Kafalas JA. Fast $Na^+$-ion transport in skeleton structures. Materials Research Bulletin. 1976;11(2):203-20.
18. Bohnke O, Ronchetti S, Mazza D. Conductivity measurements on nasicon and nasicon-modified materials. Solid State Ionics. 1999;122(1–4):127-36.

19. Essoumhi A, Favotto C, Mansori M, Satre P. Synthesis and characterization of a NaSICON series with general formula $Na_{2.8}Zr_{2-y}Si_{1.8-4y}P_{1.2+4y}O_{12}$ ($0 \leq y \leq 0.45$). Journal of Solid State Chemistry. 2004;177(12):4475-81.
20. Martucci A, Sartori S, Guglielmi M, Di Vona ML, Licoccia S, Traversa E. NMR and XRD study of the influence of the P precursor in sol-gel synthesis of NASICON powders and films. Journal of the European Ceramic Society. 2002;22(12):1995-2000.
21. Wang B, Liang XS, Liu FM, Zhong TG, Zhao C, Lu GY, et al. Synthesis and characterization of NASICON nanoparticles by sol-gel method. Chemical Research in Chinese Universities. 2009;25(1):13-6.
22. Zhang S, Quan B, Zhao Z, Zhao B, He Y, Chen W. Preparation and characterization of NASICON with a new sol-gel process. Materials Letters. 2004;58(1-2):226-9.
23. Zhang ZZ, Shi SQ, Hu YS, Chen LQ. Sol-gel synthesis and conductivity properties of sodium ion solid state electrolytes $Na_3Zr_2Si_2PO_{12}$. Wuji Cailiao Xuebao/Journal of Inorganic Materials. 2013;28(11):1255-60.
24. Quon DHH, Wheat TA, Nesbitt W. Synthesis, characterization and fabrication of $Na_{1+x}Zr_2Si_xP_{3-x}O_{12}$. Materials Research Bulletin. 1980;15(11):1533-9.
25. Kreuer KD, Kohler H, Warhus U, Schulz H. NASICON solid electrolytes part III: Sodium conductivity enhancement along domain and grain boundaries. Materials Research Bulletin. 1986;21(2):149-59.
26. Boilot JP, Salanié JP, Desplanches G, Le Potier D. Phase transformation in $Na_{1+x}Si_xZr_2P_{3-x}O_{12}$ compounds. Materials Research Bulletin. 1979;14(11):1469-77.
27. Di Vona ML, Traversa E, Licoccia S. Nonhydrolytic Synthesis of NASICON of Composition $Na_3Zr_2Si_2PO_{12}$: A Spectroscopic Study. Chemistry of Materials. 2001;13(1):141-4.
28. Standard Test Methods for Determining Average Grain Size. ASTM Standard E112 - 2010: ASTM International, West Conshohocken, PA; 2010.
29. Kudoh Y, Takeda H, Arashi H. In situ determination of crystal structure for high pressure phase of $ZrO_2$ using a diamond anvil and single crystal X-ray diffraction method. Physics and Chemistry of Minerals. 1986;13(4):233-7.
30. Foster MD, Friedrichs OD, Bell RG, Paz FAA, Klinowski J. Chemical evaluation of hypothetical uninodal zeolites. Journal of the American Chemical Society. 2004;126(31):9769-75.
31. Kang S-JL. 9 - Abnormal Grain Growth. Sintering. Oxford: Butterworth-Heinemann; 2005. p. 117-35.
32. Cantwell PR, Tang M, Dillon SJ, Luo J, Rohrer GS, Harmer MP. Grain boundary complexions. Acta Materialia. 2014;62(Supplement C):1-48.
33. Cantwell PR, Ma S, Bojarski SA, Rohrer GS, Harmer MP. Expanding time–temperature-transformation (TTT) diagrams to interfaces: A new approach for grain boundary engineering. Acta Materialia. 2016;106(Supplement C):78-86.
34. Haile SM, Staneff G, Ryu KH. Non-stoichiometry, grain boundary transport and chemical stability of proton conducting perovskites. Journal of Materials Science. 2001;36(5):1149-60.
35. Haile SM, West DL, Campbell J. The role of microstructure and processing on the proton conducting properties of gadolinium-doped barium cerate. Journal of Materials Research. 2011;13(6):1576-95.
36. Bonanos N, Steele BCH, Butler EP. Impedance Spectroscopy: Wiley and Sons, New York, USA; 1988.

37. McLachlan DS, Blaszkiewicz M, Newnham RE. Electrical Resistivity of Composites. Journal of the American Ceramic Society. 1990;73(8):2187-203.
38. Uvarov NF. Composite solid electrolytes: recent advances and design strategies. Journal of Solid State Electrochemistry. 2011;15(2):367-89.
39. Nan C-W, Smith DM. A.c. electrical properties of composite solid electrolytes. Materials Science and Engineering: B. 1991;10(2):99-106.
40. Guin M, Indris S, Kaus M, Ehrenberg H, Tietz F, Guillon O. Stability of NASICON materials against water and $CO_2$ uptake. Solid State Ionics. 2017;302:102-6.
41. Khireddine H, Fabry P, Caneiro A, Bochu B. Optimization of NASICON composition for $Na^+$ recognition. Sensors and Actuators B-Chemical. 1997;40(2-3):223-30.
42. Ahmad A, Wheat TA, Kuriakose AK, Canaday JD, McDonald AG. Dependence of the properties of Nasicons on their composition and processing. Solid State Ionics. 1987;24(1):89-97.
43. Fuentes RO, Figueiredo FM, Marques FMB, Franco JI. Influence of microstructure on the electrical properties of NASICON materials. Solid State Ionics. 2001;140(1-2):173-9.